



HAL
open science

Model-based skin pigment cartography by high-resolution hyperspectral imaging

Pierre Seroul, Mathieu Hébert, Marie Chérel, Romain Vernet, Raphael Clerc,
Matthieu Jomier

► To cite this version:

Pierre Seroul, Mathieu Hébert, Marie Chérel, Romain Vernet, Raphael Clerc, et al.. Model-based skin pigment cartography by high-resolution hyperspectral imaging. *Journal of Electronic Imaging*, 2016, *Journal of Electronic Imaging*, 69 (6), pp.48 - 56. hal-01458764

HAL Id: hal-01458764

<https://hal.science/hal-01458764>

Submitted on 11 Feb 2017

HAL is a multi-disciplinary open access archive for the deposit and dissemination of scientific research documents, whether they are published or not. The documents may come from teaching and research institutions in France or abroad, or from public or private research centers.

L'archive ouverte pluridisciplinaire **HAL**, est destinée au dépôt et à la diffusion de documents scientifiques de niveau recherche, publiés ou non, émanant des établissements d'enseignement et de recherche français ou étrangers, des laboratoires publics ou privés.

Model-based skin pigment cartography by high-resolution hyperspectral imaging

Pierre Seroul¹, Mathieu Hébert², Marie Chere¹, Romain Vernet¹, Raphael Clerc²,
Matthieu Jomier¹

¹Newtone Technologies, 13 bis Place Jules Ferry, F-69006 Lyon, France.

²Univ Lyon, UJM-Saint-Etienne, CNRS, Institut d'Optique Graduate School, Laboratoire Hubert Curien UMR 5516, F-42023, SAINT-ETIENNE, France.

Abstract

The determination of local components in human skin from in-vivo spectral reflectance measurements is crucial for medical applications, especially for aiding the diagnostic of skin diseases. Hyper-spectral imaging is a convenient technique since one spectrum is acquired in each pixel of the image, and by inverting a light scattering model, we can retrieve the concentrations of skin components in each pixel. The good performance of the method presented in this paper comes from both the imaging system and the model. The hyper-spectral camera that we conceived uses polarizing filters in order to remove gloss effects generated by the stratum corneum; it provides a high resolution image (1120 × 900 pixels), with a thin spectral sampling of 10 nm over the visible spectrum. The acquisition time of 2 seconds is short enough to prevent movement effects of the imaged area, which is usually the main issue in hyperspectral imaging. The model relies on a two-layer model for the skin, and the Kubelka-Munk theory with Saunderson correction for the light reflection. An optimization method enables computing, in less than one hour, several skin parameters in each of the million of pixels. These parameters (blood, melanin and bilirubin volume fractions, oxygen saturation...) are then displayed under the form of density images. Different skin structures, such as veins, blood capillaries, hematoma or pigmented spots, can be highlighted. The deviation between the measured spectrum and the one computed from the fitted parameters is evaluated in each pixel.

1. Introduction

Skin chromophores and their influence on skin color perception are a major concern in dermatology and cosmetics in order to evaluate pigmentation issues [1-3]. Non-invasive imaging systems of the skin are used in a wide range of clinical applications in the last decades, in particular in order to get information on pigmentation disorders: melanin index, port wine vein, vitiligo, erythema [4-5]... Since pigmentation determines the spectral reflectance of the skin, the best way to observe it is to make images in different spectral bands, either in three wide spectral bands as in classical RGB imaging [6-7], or in more than 10 short spectral bands as in multispectral imaging [8-9]. There already exist several multispectral imaging instruments for skin observation on the marketplace (e.g. SIAscope from Astron Clinica Limited, or MelaFind from Mela Sciences, ...) generally dedicated to specific measurements. In the present study, we used the hyper-spectral camera that we developed and presented in Section 2, SpectraCam®, whose

spectral and spatial resolutions are higher than the aforementioned ones, thus permitting more accurate skin analysis.

The concentration and localization of chromophores and photophores in the skin cannot be measured directly by optical device, but they can be deduced from light signal captured by the imaging system, by using a spectral reflectance model for the skin taking into account the spectral absorbance of the chromophores [10]. Two main approaches are usually followed in the literature: Monte-Carlo simulation, and 2-flux models. The Monte-Carlo method consists in a stochastic stimulation of light paths in the skin with multiple interactions with scatterers [1,12-15]. The drawback of this method is that it cannot be easily reversed in order to deduce skin parameters from measured spectra [16]: several minutes are needed for treating one spectrum, even with fastened methods such as the adaptive method proposed by Spanier [17]. The two-flux models rely on a physical model of light propagation which can be seen as a special solution of the radiative transfer equation, standing in case of strong scattering. The Kubelka-Munk model predicts the reflectance and transmittance of one homogeneous layer as a function of its thickness [18], and the Kubelka compositional model can predict the reflectance and transmittance of stacks of homogenous layers [19]. Two-flux models have been used in a wide range of applications, included skin analysis [3,20-22], most of the time without Saunderson correction [23], which means that the optical effect of the air-skin interface is not taken into account. More advanced models describe more thinly the scattering of light by the skin tissues, especially the angular distribution of the scattered light, thanks to methods based on the radiative transfer theory with a multilayer model [16,24-25]. This approach is physically more rigorous but difficult to use in practice due to the needed computation time for computing the parameters from bi-directional spectral reflectance measurements. The number of parameters should be also restricted in order to guarantee uniqueness of the solution in the optimization process [26].

The method that we present in this paper relies on the Kubelka-Munk model with Saunderson correction (Section 3), by considering the simplified model for skin tissues presented in Section 4. The inversed model, fastened by an optimized algorithm, enables computing rather fast five skin parameters: epidermis depth, melanin volume fraction, blood volume fraction, oxygen saturation and bilirubin volume fraction. These parameters can be displayed under the form of density maps [3]. The estimation error between simulated and real spectrum is computed using least square and spectral angle similarity (SAS) [27]. In order to verify the performance of the method, acquisitions were made on ten Caucasian skins to correlate results reported by previous works [28- 29] and pigment maps were compared to literature [11] (Section 6).

2. Hyperspectral imaging system

The imaging system that we used is a modular device for hyperspectral imaging, SpectraCam®, developed by Newton Technologies, France. In its standard mode, it can capture up to 31 images in different thin wavebands of the visible spectrum (400–700 nm), every 10 nm. For specific clinical applications, it can also capture one image every 1

nm through a spectral band of 10 nm. The surface is illuminated at approximately 8° from its normal by four large visible band power LEDs symmetrically disposed around optical axis (see Figure 1). The acquisition time for each waveband is selected in order to prevent saturation while ensuring good signal-to-noise ratio. The total acquisition time for the 31 images is 2.5 seconds, which is appreciable for measurements on alive surfaces: the risk of movement is rather low, and the images corresponding to the different wavelengths are most often perfectly registered with each other.

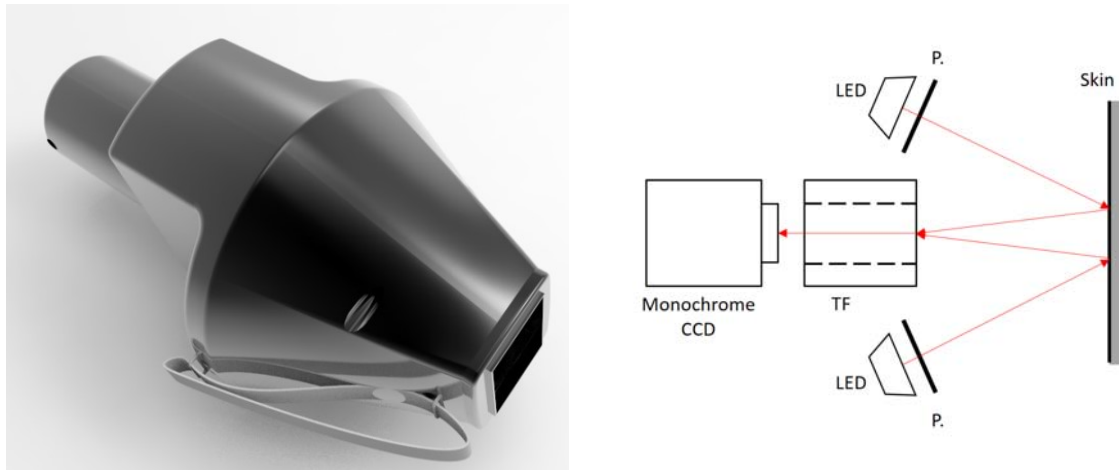


Figure 1 – SpectraCam (left) and its schematic (right). Light emitted by LEDs is transmitted through the polarizers (P.) and reflected by the skin. A tunable filter (TF) let pass a specific wavelength and is used as analyzer. The resulting image is captured by a monochromatic camera.

In order to avoid artifacts due to the specular reflection of light by the skin surface (gloss), the system integrates two polarization filters, one for polarizing the incident light, another one for the reflected light. This system uses the fact that when the incident light is polarized, the light reflected by the surface of a dielectric medium has similar polarization as the incident light, whereas the light scattering into the diffusing medium is unpolarized. Thus, when the second polarizing filter is parallel to the first one (Parallel-Polarization mode, hereinafter denoted as PP), it transmits both the specularly and diffusely reflected light components. When it is perpendicular to the first filter (Cross-Polarization mode, CP), it transmits only the diffused light, without the specularly reflected component (see Figure 2).

For an analysis of the pigment composition of the skin, the CP mode is preferable since information is deduced from the spectral distribution of the diffusely reflected light. The PP mode is useful for an analysis of the skin surface structure, highlighted by the specular reflectance. Note that the specular reflected light can be computed by subtracting the CP-image to the-PP image.



Figure 2 – Same skin area observed by the hyperspectral imaging system in cross-polarization mode (left) or parallel-polarization mode (center); subtracting the two images yields the gloss image displayed on the right. Here, hyperspectral images are converted into RGB color images.

The SpectraCam® device also enables analyzing fluorescence emission by photophores thanks to a UV-A lamp emitting around 365 nm. 31 images are captured corresponding to the same wavelengths as for the chromophores analysis. When the UV lamp is on and the white light off, the measured spectrum corresponds to the fluorescence emittance. This mode is not used in the present study.

The repeatability of the spectral measurement system is similar to spectrophotometers used in color reproduction: the standard deviation over 10 measurements on a same white ceramic, expressed in CIELAB 1976 ΔE^*_{ab} , is 0.09 unit with our system, therefore comparable to the Konica Minolta CM-700d instrument (0.04 unit on the same sample) and the X-Rite SP62 instrument (0.05 unit).

3. Kubelka-Munk model and Saunderson correction

The Kubelka-Munk model describes the propagation of diffuse natural light within a layer of homogenous scattering and absorbing medium, characterized by its thickness h , its linear absorption coefficient K and its linear backscattering coefficient S [18]. The fluxes i and j propagating respectively forwards and backwards within the layer satisfy at every depth z the following system of differential equations

$$\begin{cases} \frac{di}{dz} = -(K + S) i(z) + S j(z) \\ \frac{dj}{dz} = -S i(z) + (K + S) j(z) \end{cases} \quad (1)$$

By integrating these differential equations [31], one obtains the following expressions for the reflectance R and the transmittance T of the layer:

$$R = \frac{\sinh(bSh)}{b \cosh(bSh) + a \sinh(bSh)}, \quad (2)$$

and

$$T = \frac{b}{b \cosh(bSh) + a \sinh(bSh)}, \quad (3)$$

with

$$a = (K + S) / S \quad \text{and} \quad b = \sqrt{a^2 - 1} \quad (4)$$

As the layer thickness tends to infinity, the reflectance tends to the limit

$$R_\infty = a - b = \frac{K + S - \sqrt{K(K + 2S)}}{S} \quad (5)$$

and the transmittance obviously trends to 0.

When the layer is on top of an opaque background with reflectance ρ_g , the reflectance becomes [31]

$$R_g = \frac{(1 - a\rho_g) \sinh(bSh) + b\rho_g \cosh(bSh)}{(a - \rho_g) \sinh(bSh) + b \cosh(bSh)} \quad (6)$$

Note that since absorption and scattering coefficients generally depend on wavelength, all reflectance and transmittance expressions also depend on wavelength.

Most of the time, the refractive index of the layer is different from the one of the surrounding medium, e.g., air. The reflectance R_g of the layer with background, expressed by Eq. 6, is thus transformed into the following one

$$R_S = r_s + \frac{T_{in} T_{out} R_g}{1 - r_i R_g} \quad (7)$$

where the terms r_s , T_{in} and T_{out} are derived from the Fresnel formulas according to the measuring geometry [32]. This expression generalizes the Saunderson correction for the Kubelka-Munk model for any measuring geometry (in his original paper, Saunderson considered illumination at 45° from the normal of the layer, and observation in the normal of the layer [23]). For the $8^\circ:0^\circ$ geometry, one has

$$\begin{aligned} r_s &= 0 \\ T_{in} &= T_{fresnel}(8^\circ) = 1 - R_{fresnel}(8^\circ) \\ T_{out} &= T_{fresnel}(0^\circ) / n^2 \end{aligned} \quad (8)$$

Where n is the refractive index of the layer and the factor $1/n^2$ introduces the fact that the captured radiance has been spread into a larger cone when crossing the interface due to refraction [32]. Note that $r_s = 0$ because the incident and reflection are different; it is also zero when the specular reflection is removed by polarization filtering. Moreover, it has been shown that T_{in} , T_{out} and r_i are almost not modified by eventual roughness of the surface [33].

4. Simplified skin model

Human skin has a multilayer structure, each layer having specific optical properties. Depending on the optical model that is used, the considered number of layers is 2, 3, 5, 7, or even more (Refs. [34], to [38], respectively). Anderson [20] considers a two-layer system: epidermis, which contains melanin, and dermis, containing collagen fibers as scatterers, and blood and its derivatives as absorbers, among which hemoglobin (Hb), oxyhemoglobin (HbO₂), bilirubin, as well as β -carotene. We adopted similar two-layer

structure (see Figure 3). We considered the epidermis as a diffusing layer with refractive index $n = 1.4$, thickness h , absorption coefficient K_e and scattering coefficient S_e , and the dermis as a diffusing layer with absorption coefficient K_d and scattering coefficient S_d . The dermis thickness is assumed infinite and its refractive index identical to the one of the epidermis. For this structure where a diffusing layer is on top of a background, Eq. 7 applies. Surprisingly, the optical effect of the air-skin interface (here modeled by the Saunderson correction) is ignored in most works referred to in this paper, except in Ref. [25] where specific bounding conditions are used in the auxiliary function method for solving of the radiative transfer equation. Ignoring the reflections and refractions of light at the skin surface is in contradiction with the optical laws and introduces significant error in the skin reflectance model.

For the spectral scattering coefficients of the epidermis and dermis, and the spectral absorption coefficients of the skin pigments used in our model, we referred to Ref. [28]. The absorption coefficients of the two layers depend on the pigments contained in them and their respective volume fraction: According to the Beer-Lambert-Bouguer law [39], the spectral absorption coefficient of the absorber mixture is a linear, additive combination of the spectral absorption coefficients of the individual absorbers, weighted by their respective concentration [40]

The epidermis contains a baseline with absorption coefficient $K_b(\lambda)$, and melanin with absorption coefficient $K_m(\lambda)$ and volume fraction c_m . The absorption coefficient of the epidermis is therefore

$$K_e(\lambda) = (1 - c_m)K_b(\lambda) + c_mK_m(\lambda) \quad (9)$$

With this absorption coefficient $K_e(\lambda)$ and the scattering coefficient $S_e(\lambda)$, the reflectance R_e and transmittance T_e of the epidermis can be computed as a function of its thickness h by using Eqs.2 and 3.

The dermis contains the same baseline as the epidermis [absorption coefficient $K_b(\lambda)$], deoxy-hemoglobin Hb (absorption coefficient $K_{Hb}(\lambda)$ and volume fraction c_{Hb}), oxy-hemoglobin Hb02 ($K_{Hb02}(\lambda)$, c_{Hb02}) and bilirubin ($K_{bi}(\lambda)$, c_{bi}):

$$K_d(\lambda) = c_bK_b(\lambda) + c_{Hb}K_{Hb}(\lambda) + c_{Hb02}K_{Hb02}(\lambda) + c_{bi}K_{bi}(\lambda) \quad (10)$$

with $c_b = 1 - (c_{Hb} + c_{Hb02} + c_{bi})$. With this absorption coefficient K_d and the scattering coefficient S_d , the reflectance R_d of the dermis can be computed using Eq. 5.

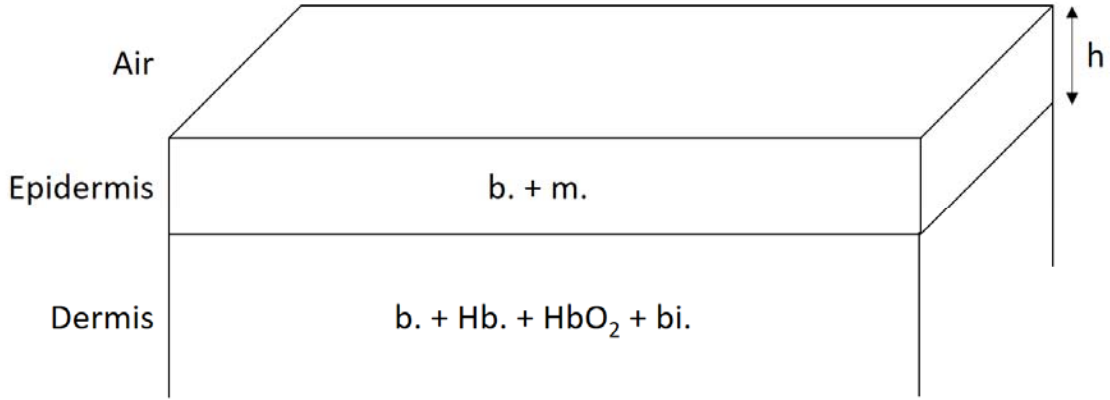


Figure 3. Skin model with two layers. Epidermis is composed of baseline (b.) and melanin (m.) and has a thickness h . Dermis is composed of baseline (b.), deoxy-hemoglobin (Hb.), oxy-hemoglobin (HbO₂) and bilirubin (b.). Its thickness is assumed to be infinite.

5. Model inversion for the computation of the skin parameters

The spectral reflectance of the skin is given by Eq. 7, with $R_g(\lambda)$ given by Eq. 6. In the expression for $R_g(\lambda)$, the background reflectance $\rho_g(\lambda)$ is replaced with the dermis reflectance $R_d(\lambda)$ expressed by Eq. 5 as a function of $S_d(\lambda)$ and $K_d(\lambda)$ (Eq. 10); the reflectance R and transmittance T of the epidermis are respectively expressed by Eqs. 2 and 3 as functions of $S_e(\lambda)$ and $K_e(\lambda)$ (Eq. 9). For each pixel of the hyperspectral image, one fits the pigment concentrations and the epidermis thickness as values for which the error between the spectrum $R_p(\lambda)$ predicted by our reflectance model and the measured spectrum $R_m(\lambda)$ is minimal. Two errors were implemented as cost function to optimize the model, a classical least square error (Eq. 11) and the Spectral Angle Similarity (SAS) (Eq. 12) [41]:

$$\{c_m, c_{Hb}, c_{HbO_2}, c_{bi}, h\} = \underset{c_m, c_{Hb}, c_{HbO_2}, c_{bi}, h}{\operatorname{argmin}} \sum (R_p(\lambda) - R_m(\lambda))^2 \quad (11)$$

$$\{c_m, c_{Hb}, c_{HbO_2}, c_{bi}, h\} = \underset{c_m, c_{Hb}, c_{HbO_2}, c_{bi}, h}{\operatorname{argmin}} \arccos \left(\frac{\sum R_p(\lambda) R_m(\lambda)}{\left[\sum R_p^2(\lambda) \right] \left[\sum R_m^2(\lambda) \right]} \right) \quad (12)$$

The optimization yielding the parameter values relies on the Nelder-Mead method [42]. The fact that the different pigments have different absorption bands insures a unique solution for this optimization process. In order to verify the stability of the obtained values of parameters, we introduced small variations in the hyperspectral image and observed that the variations of the parameter values were low. Moreover, we could verify that a bijective relationship exists between the parameter values and the reflectance spectra, which means that the model can be reversed. This enables attributing a unique set of parameters to every reflectance spectrum of skin. The five parameters are computed for each of the 1 008 000 pixels in less than one hour (3.4 ms per pixel). The computation speed optimization that has been achieved is an advantage for medical

applications: it remains important for immediate clinical diagnosis but is acceptable for offline data evaluation in the context of clinical trials.

From the obtained set of parameters, one may compute again the skin reflectance and compare it to the measured ones. This enables assessing the relevance of the parameter values and the accuracy of the model. The deviations may come from the presence of other pigments, non-modeled optical phenomena, or local variations of the optical properties of the skin which are not taken into account in our model. The SAS metric is computed for each pixel of the image and can be also displayed under the form of a density images.

6. Experimental testing

Clinical experiments were performed onto 10 Caucasian subjects with phototypes I (fair skin) to III (light brown skin) on the Fitzpatrick scale [43-44], 5 males and 5 females between 20 and 50 years old. Seven areas of interest were observed on each subject, located on the right and left inner forearms, on the right and left cheeks and on the forehead. This makes a set of 70 hyperspectral images. The size of each area is 5 cm x 4 cm (1120 × 900 pixels). The SAS value has been shown to be less sensitive than least square error to irradiance variation across the image, especially visible on oxygen saturation maps (Figure 4).

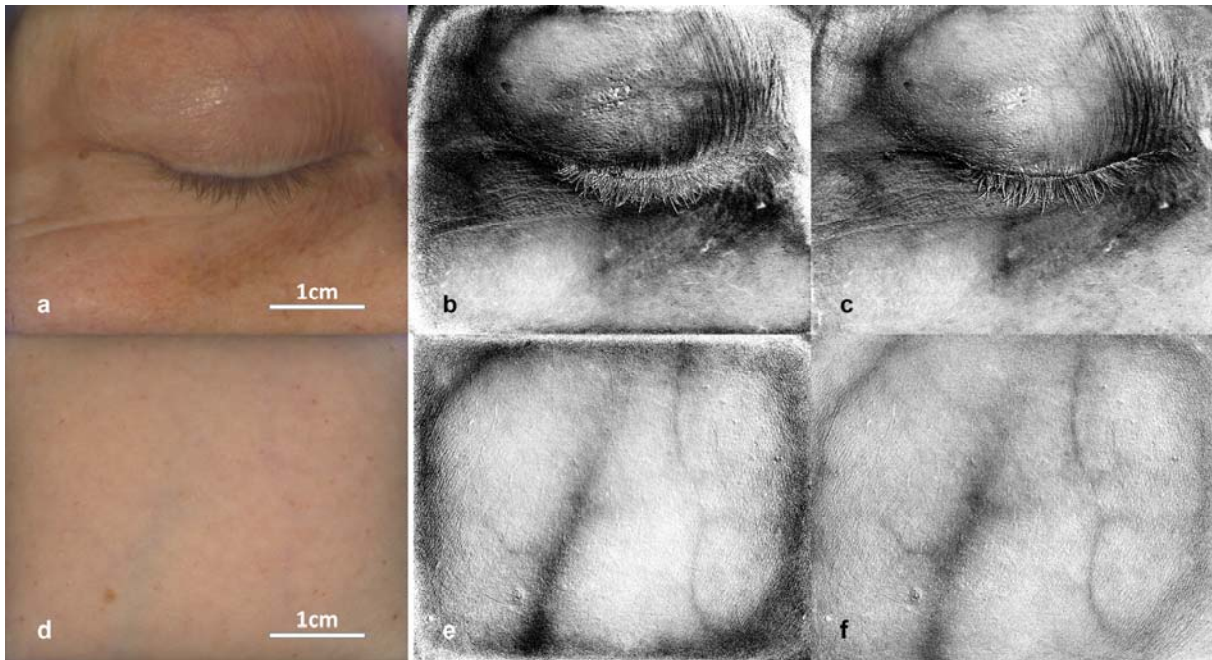


Figure 4. Color images (a and d), and oxygen saturation images reconstructed using a least square cost function (b and e) and a SAS cost function (c and f)

Computed over all pixels of the 70 hyperspectral images, the SAS value was 0.044, which is of the same order as the value 0.017 given in Ref. [3] where this value can theoretically vary from 0 to $\Pi/2$. Average skin parameters and their standard deviation, obtained from the 70 hyperspectral images, are given in Table 1. Except from the

epidermis thickness that is overestimated compared to literature, all parameters fit in the range detailed in previous works. An originality of our study is the estimation of the bilirubin volume fraction by hyperspectral imaging.

Table 1. Skin parameters estimated from 7 areas on 10 Caucasian subjects

Skin Parameter	Estimated value*	Data from the literature
Epidermis thickness	$41 \pm 8 \mu\text{m}$	$34 \pm 4 \mu\text{m}$ [45]
Melanin volume fraction	$15 \pm 5.7\%$	1.3 – 43% [28]
Blood volume fraction	$5.5 \pm 3.7\%$	2 – 5% [28]
Oxygen saturation	$50 \pm 15\%$	25–90% [46]
Bilirubin volume fraction	$0.35 \pm 0.15\%$	0.3–1.2 mg/dL [47]**

*Average over the 10 Caucasian subjects and standard deviation

**This concentration of bilirubin is measured in serum whereas our measurement is an effective volume fraction in the skin

We compared our method with the method proposed by Stamatas et al., a reference work in the literature in which spectral data are used to estimate melanin, oxy-hemoglobin and deoxy-hemoglobin [11]. In both methods, we combined oxy- and deoxy-hemoglobin in order to obtain blood and oxygenation values. Blood map is defined as the sum of oxy- and deoxy-hemoglobin concentrations and oxygenation as the ratio between oxy-hemoglobin and blood concentrations.

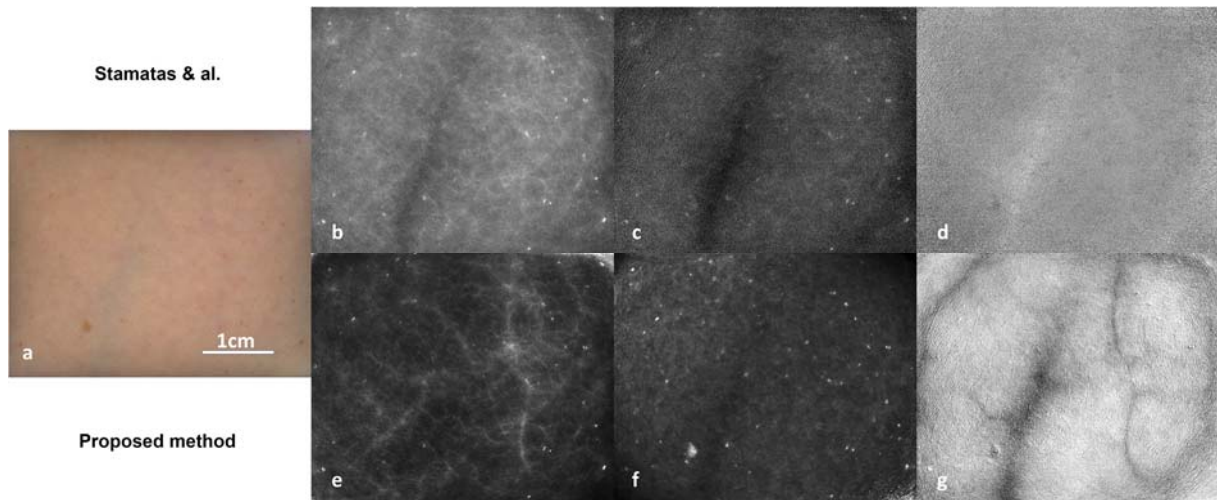


Figure 5 – Color image (a) and blood (b), melanin (c) and oxygen (d) maps implemented using Stamatas & al. method [11] compared with blood (e), melanin (f) and oxygen (g) maps with the proposed method.

Blood capillaries network is roughly visible using Stamatas & al (Figure 5.b) whereas it is more clearly defined with the proposed method (Figure 5.e). Some pigmented spots, visible in the color image are not identifiable in the Stamatas & al melanin maps (Figure 5.c) whereas they are well defined in the proposed method (Figure 5.f). Furthermore, with the proposed method, some of the spots can be differentiated between the ones visible only on the melanin image and the ones visible both in the melanin and blood images. Finally, with the proposed method, oxygenation map displays clearly veins network (Figure 5.g) whereas they generate artefacts in blood and melanin maps (Figure 5.b and Figure 5.a) and are not visible in oxygenation maps (Figure 5.d) using the method by Stamatas & al.

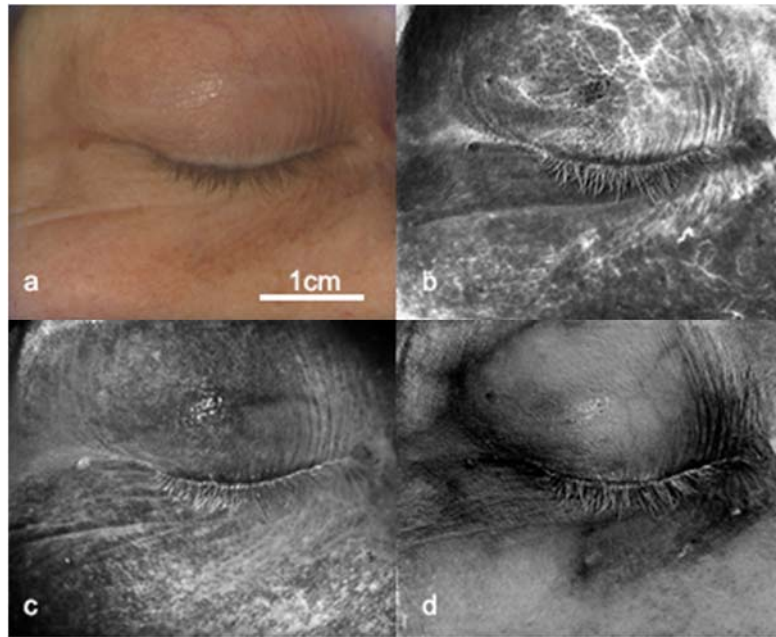


Figure 6. Color image (a), and density images of blood volume fraction (b), oxygen saturation (c) and melanin volume fraction (d) issued from a hyperspectral image of female eye contour (courtesy of Clarins S.A).

Figure 6 shows another example of observed skin area, with a color image and relevant grey-level images representing density images for three skin parameters: the whole eyelid and eye contour blood irrigation in well described in the blood image (Figure 6.b). The dark circle is well defined on the oxygen saturation image (Figure 6.d). The melanin image (Figure 6.a) shows no specific variations around the eye helping the diagnosis between dark circles due to oxygenation issues and eye contour hyper-pigmentation.

7. Conclusions

The method presented in this paper enables quantitative estimation of pigment concentrations in each point of a given area of human skin, and therefore display of their spatial distribution. The good performance of the method comes from the combination of a high-resolution hyper-spectral imaging system with polarizing filters, and an inverse model based on the two-flux theory (Kubelka-Munk model in a two-layer structure for the skin, with Saunderson correction in order to take into account the internal reflections of light at the skin-air interface). The use of cross-polarization enables removing light reflections of the stratum corneum, which may be an important error factor in chromophores quantification. The model allows retrieving six parameters of Caucasian skin: epidermis depth, melanin volume fraction, blood volume fraction, oxygen saturation and bilirubin volume fraction. The estimation of this latter parameter is an originality of our work compared to the existing works. Images of each of these parameters can be displayed to observe different structures such as veins, blood capillaries, hematoma or pigmented spots. A spectral deviation image is also displayed to highlight structures that do not fit well with the developed skin model. From the tests carried out in this study, we observed good agreement between estimated parameter values with our system and those available in the literature. In the future, we would like

to validate the estimated parameters values with specific protocols in which their variations are under control.

References

1. Preece, S.J., Claridge, E., "Spectral filter optimization for the recovery of parameters which describe human skin." *IEEE Trans. Pattern Anal. Mach. Intell* **26**, 913–922 (2004).
2. Cotton, S., "A noninvasive skin imaging system", in *Information Processing in Medical Imaging*, Duncan J. and Gindi G. Eds., *Lecture Notes in Computer Science* **1230**, Springer, Berlin, pp. 501-506 (1997).
3. Jolivot, R., Benezeth, Y., Marzani, F., "Skin Parameter Map Retrieval from a Dedicated Multispectral Imaging System Applied to Dermatology/Cosmetology," *Int. J. Biomedical Imaging* **2013**, Article 978289 (2013).
4. Nilsson, G., "Tissue Viability Imaging for Assessment of Skin Erythema and Blanching" *Non Invasive Diagnostic Techniques in Clinical Dermatology*, 187-199 (2014).
5. Jung, B., Choi, B., Durkin, A.J., Kelly, K.M., Nelson, J.S., "Characterization of Port Wine Stain Skin Erythema and Melanin Content Using Cross-Polarized Diffuse Reflectance Imaging," *Lasers in Surgery and Medicine* **34**, 174-181 (2004).
6. Liu, Z., Zerubia, J. "Melanin and Hemoglobin Identification for Skin Disease Analysis." *IEEE proceedings of Asian Conference on Pattern Recognition (ACPR)*, Nov 2013, Okinawa, Japan (2013).
7. Tsumura N., Haneiski H., Miyake Y., "Independent-component analysis of skin color image" *J. Opt. Soc. Am. A* **16** (9), 2169-2176 (1999)
8. Elbaum, M., "Computer-Aided Melanoma Diagnosis" *Dermatologic Clinics* **20**, 735-47 (2002).
9. Tsumura N., Kawabuchi M., Haneiski H., Miyake Y., "Mapping pigmentation in human skin from a multi-channel visible spectrum image by inverse optical scattering technique" *Journal of Imaging Science and Technology* **45** (5), 444-450 (2001)
10. Stamatas, G.N., Zmudzka, B. Z., Kollias, N., Beer, J. Z., "Non-invasive measurements of skin pigmentation in situ". *Pigment Cell Res.* **17**, 618–626 (2004).
11. Stamatas G. N., Zmudzka B.Z., Kollias N., Beer J.Z., "In vivo measurement of skin erythema and pigmentation: New means of implementation of diffuse reflectance spectroscopy with a commercial instrument", *British Journal of dermatology* **159**, 683-690 (2008)
12. Meglinski, I.V., Matcher, S. J., "Computer simulation of the skin reflectance spectra," *Computer Methods and Programs in Biomedicine* **70**, 179–186 (2003).
13. Nishidate, I., Aizu, Y., Mishina, H., "Estimation of melanin and hemoglobin in skin tissue using multiple regression analysis aided by monte carlo simulation." *J. Biomed. Opt.* **9**, 700-710 (2004).
14. Shi, T., Dimarzio, C.A., "Multispectral method for skin imaging development and validation," *App. Opt.* **46**, 8619–8626 (2007).
15. Hirose M., Kuroshima M., Tsumura N., "Nonlinear estimation of chromophore concentrations, shading and surface reflectance from five band images" *Color and Imaging Conference 2015*(1), 161-166 (2015)
16. Zhang, R., Verkruysse, W., Choi, B., Viator, J.A., Jung, B., Svaasand, L.O., Aguilar, G., Nelson, J. S., "Determination of human skin optical properties from spectrophotometric measurements based on optimization by genetic algorithms," *J. Biomed. Opt.* **10** 024030 (2005).
17. Spanier, J., "Geometrically convergent learning algorithms for global solutions of transport problems," *Proc. Monte Carlo Quasi-Monte Carlo Methods 1998*, H. Niederreiter and J. Spanier, Eds., pp. 98–113, Springer-Verlag, Berlin, Germany (2000).
18. Kubelka, P. "New contributions to the optics of intensely light-scattering material, part I," *J. Opt. Soc. Am.* **38**, 448–457 (1948).
19. Kubelka, P. "New contributions to the optics of intensely light-scattering material, part II: nonhomogeneous layers," *J. Opt. Soc. Am.* **44**, 330–335 (1954).
20. Anderson, R.R., Parrish, J.A., "The optics of human skin," *J. Invest. Dermatol.* **77**, 13-9 (1981).
21. Krishnaswamy A.G., Baranoski, V.G., "A biophysicallybased spectral model of light interaction with human skin," *Computer Graphics Forum* **23**, 331–340 (2004).

22. Igarashi, T., Nishino, K., Nayar, S. K., "The appearance of human skin: A survey," *Found. Trends. Comput. Graph. Vis.*, **3** (1), 1–95 (2007).
23. Saunderson, J.L., "Calculation of the color pigmented plastics," *J. Opt. Soc. Am.* **32**, 727–736 (1942).
24. Prahl, S. A., "Light transport in tissues", PhD dissertation, University of Texas (2008).
25. Magnain, C., Elias, M., Frigerio, J.M., "Skin color modeling using the radiative transfer function solved by the auxiliary function method," *J. Opt. Soc. Am. A* **24**, 2196–2205 (2007).
26. Zonios, G., Dimou, A., "Modeling diffuse reflectance from semi-infinite turbid media: application to the study of skin optical properties," *Opt. Express* **14**, 8661-8674 (2006).
27. Yuhas, R., Goetz, A., Boardman, J. "Discrimination among semi-arid landscape endmembers using the spectral angle mapper (sam) algorithm" *Summaries of the Third Annual JPL Airborne Geoscience Workshop*, I (JPL Publication 92-14), 147–149 (1992).
28. Jacques, *Skin optics*. Oregon Medical Laser Center News (1998).
29. Huzaira, M., Rius, F., Rajadhyaksha, M., Anderson, R., Gonzalez, A., "Topographic Variations in Normal Skin, as Viewed by In Vivo Reflectance Confocal Microscopy," *The journal of Investigative Dermatology* **116** (6), 846–852 (2001).
30. Vasefi, F., MacKinnon, N., Saager, R.B., Durkin, A.J., Chave, R., Lindsley, E.H., Farkas, D.L. "Polarization-Sensitive Hyperspectral Imaging in vivo: A Multimode Dermoscope for Skin Analysis," *Scientific Reports* **4**, paper 4924 (2014).
31. Hébert, M., Hersch, R.D., Emmel, P., "Fundamentals of Optics and Radiometry for Color Reproduction" in *Handbook of Digital Imaging*, Ed. Mickael Kriss, Wiley, New York, 1021–1077 (2015).
32. Simonot, L., Hébert, M., Hersch, R.D. "Extension of the Williams-Clapper model to stacked nondiffusing colored layers with different refractive indices," *J. Opt. Soc. Am. A* **23**, 1432–1441 (2006).
33. Hébert, M., Hersch, R.D., "Extending the Clapper–Yule model to rough printing supports," *J. Opt. Soc. Am. A* **22**, 1952–1967 (2005).
34. Kim, A.D., Moscoso, M., "Light transport in two-layer tissues," *Journal of Biomedical Optics*, vol. 10, no. 3, Article 034015 (2005).
35. Svaasand, L.O., Norvang, L.T., Fiskerstrand, E.J., Stopps, E.K.S., Berns, M.W., Nelson, J. S. "Tissue parameters determining the visual appearance of normal skin and port-wine stains," *Lasers in Medical Science* **10**, 55–65 (1995).
36. Douven, L.F.A., Lucassen, G.W. "Retrieval of optical properties of skin from measurement and modeling the diffuse reectance," *Laser-Tissue Interaction* **3914**, 312–323 (2000).
37. Meglinski, I.V., Matcher, S.J., "Quantitative assessment of skin layers absorption and skin reflectance spectra simulation in the visible and near-infrared spectral regions," *Physiological Measurement* **23**, 741–753, (2002).
38. Magnain, C., Elias, M. , Frigerio, J.-M., "Skin color modeling using the radiative transfer equation solved by the auxiliary function method: inverse problem," *J. Opt. Soc. Am. A* **25**, 1737–1743 (2008).
39. Wyszecki, G., Stiles, W.S., *Color science: Concepts and methods, quantitative data and formulae*, Wiley, New York, 2nd edition, 1982.
40. Kortüm, G., *Reflectance Spectroscopy, Principles, Methods, Applications*, Springer-Verlag, Berlin, 1969.
41. Kruse, F.A., Boardman, J.W., Lefkoff, A.B., Heidebrecht, K.B., Shapiro, A.T., Barloon, P.J., Goetz, A.F.H., "The Spectral Image Processing System (SIPS)—interactive visualization and analysis of imaging spectrometer," *Data. Remote Sens. Environ.* **44**, 145-163 (1993).
42. Nelder, J. A., Mead, R., "A simplex method for function minimization". *Computer Journal* **7**, 308–313 (1965).
43. Fitzpatrick, T. B., "Soleil et peau", *J. Médecine Esthétique* **2**, 33–34 (1975) (in French).
44. Fitzpatrick, T. B., "Ultraviolet-induced pigmentary changes: Benefits and hazards", *Therapeutic Photomedicine* **15**, 25-38 (1986).
45. Corcuff, P., Bertrand, C., Lévêque, J.L., "Morphometry of human epidermis in vivo by real-time confocal microscopy." *Arch Dermatol Res.* **285**, 475–481 (1993).
46. Meglinsky, I., Matcher, S. "Modelling the sampling volume for skin blood oxygenation measurements," *Medical and Biological Engineering and Computing* **39**, 44–50 (2001).
47. Puppalwar, P.V., Goswami, K., Dhok, A. "Evolution of Methods of Bilirubin Estimation," *Journal of Dental and Medical Sciences* **1** (3), 17-28 (2012).